

Back-Projection Pipeline

Pablo Navarrete Michelini,¹ Hanwen Liu,¹ Yunhua Lu,¹ Xingqun Jiang,¹

¹BOE Technology Co., Ltd.

Abstract

We propose a simple extension of residual networks that works simultaneously in multiple resolutions. Our network design is inspired by the iterative back-projection algorithm but seeks the more difficult task of learning how to enhance images. Compared to similar approaches, we propose a novel solution to make back-projections run in multiple resolutions by using a data pipeline workflow. Features are updated at multiple scales in each layer of the network. The update dynamic through these layers includes interactions between different resolutions in a way that is causal in scale, and it is represented by a system of ODEs, as opposed to a single ODE in the case of ResNets. The system can be used as a generic multi-resolution approach to enhance images. We test it on several challenging tasks with special focus on super-resolution and raindrop removal. Our results are competitive with state-of-the-arts and show a strong ability of our system to learn both global and local image features.

Introduction

Image enhancement is the process of taking an impaired image as input and return an image of better quality. The current trend to achieve this target is to learn a mapping between impaired and enhanced images using example data. Deep-learning is leading this fast-growing quest in a number of applications, including: denoise (Lefkimmatis 2018), deblur (Tao et al. 2018), super-resolution (Timofte et al. 2018), demosaicking (Kokkinos and Lefkimmatis 2018), compression removal (Lu et al. 2018), dehaze (Ancuti et al. 2018b), derain (Wang et al. 2019), raindrop removal (Qian et al. 2018a), HDR (Wu et al. 2018), and colorization (He et al. 2018). Progress in network architectures often succeeds in image enhancement, as seen for example in image super-resolution, with CNNs applied in SRCNN (Dong et al. 2014), ResNets (He et al. 2016) applied in EDSR (Lim et al. 2017), DenseNets (Huang et al. 2017) applied in RDN (Zhang et al. 2018d), attention (Hu, Shen, and Sun 2018) applied in RCAN (Zhang et al. 2018a), and non-local attention (Wang et al. 2018) applied in RNAN (Zhang et al. 2019). In all these examples, arguably the most influential practice is the use of residual networks (ResNets). Here, we define the *network state* as the internal representation of an image in a network, commonly referred to as latent or feature space in the literature. The idea of ResNets is to represent an impaired image as a network state and progressively change it

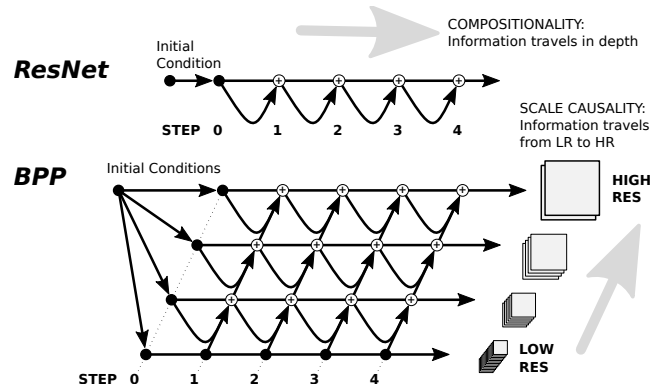


Figure 1: Our system (BPP) works as a multi-scale ResNet with state updates that interact with lower resolution states. Information travels forward in depth and upwards in scale.

by adding residuals, as seen in Figure 1. This gives a compositional hierarchy (Poggio et al. 2017) of progressive local processing steps (e.g. convolutional layers) that transforms the input image. The update strategy of residual networks can be seen as a dynamical system where depth represents time and a differential equation models the evolution of the state (Liao and Poggio 2016).

Our proposed system, a **Back-Projection Pipeline (BPP)**, works as a residual network that carries many (instead of one) resolution states at a given time step as seen in Figure 1. Although similar in spirit to U-Nets (Ronneberger, Fischer, and Brox 2015), this multi-resolution state is fundamentally different. U-Nets hold high resolution states to re-enter the network in later stages, whereas in BPP the state is created as initial conditions in multiple resolutions and get updated synchronously through the network. Another distinctive property of BPPs is *scale causality*. Namely, after initialization, low resolution states do not depend on higher resolution states. Information travels forward in depth, same as in ResNets, and upwards in scale, as shown in Figure 1. Scale causality is inspired by scale-space (Lindeberg 1994) and multi-resolution analysis (Mallat 1998) to express the nested nature of details. A simple example is that when we see an image of a keyboard we expect to see letters, but not necessarily the other way around. Finally, the interpretation

of BPPs as an extension of ResNets becomes more clear from the dynamic of the network. We will show that BPP updates can be modeled by a non-autonomous system of differential equations, as opposed to a single ODE for ResNets.

Related Work. With regard to applications, BPP gives us a generic multi-resolution approach to transform images into a desired target. Current benchmarks in image enhancement often use different architectures for different tasks. It is important to distinguish between local and global targets. In the problem of super-resolution, for example, we need to calculate pixel values around a local area, and distant pixels become less relevant. In a different problem, contrast enhancement, we want to change the histogram of an image, which contains statistics that represent global features. General image enhancement is gaining interest in research and has been considered in the context of:

- *Mixed Local Problems:* In (Zhang et al. 2019), for example, authors solve denoising, super-resolution and deblur tasks using a single architecture and different parameters for each problem. In (Gharbi et al. 2016; Ehret et al. 2019) authors solve joint demosaicking and denoising, and in (Qian et al. 2019) authors additionally solve super-resolution, all through using a single architecture and same model parameters. In (Zhang, Zuo, and Zhang 2018) authors tackle super-resolution and deblur, and train a single system to handle different image degradations.
- *Global and Local Problems:* Authors in (Soh, Park, and Cho 2019; Kim, Oh, and Kim 2019; Kinoshita and Kiya 2019) consider the joint solution of low-to-high dynamic range enhancement as well as image-SR. In (Kim, Oh, and Kim 2019) authors generate an image in HDR display format, whereas (Soh, Park, and Cho 2019; Kinoshita and Kiya 2019) use the same input and output format. They both use U-Net configurations, while (Soh, Park, and Cho 2019) uses a two-stage Retinex decomposition network.

Regarding architecture, BPP uses a multi-resolution workflow, which is different from U-Nets (Ronneberger, Fischer, and Brox 2015). This workflow follows from the Iterative Back-Projection (Irani and Peleg 1991) (IBP) algorithm. In this respect, Multi-Grid Back-Projection (Navarrete Michelini, Liu, and Zhu 2019) (MGBP) is the closest super-resolution system that is state-of-the-art for lightweight systems with small number of parameters. It is based on a multi-resolution back-projection algorithm that uses a multigrid recursion (Trottenberg and Schuller 2001). This recursion violates scale-causality as it sends network states back to low-resolution to restart iterations. We also notice that BPP follows the wide-activation design in (Yu et al. 2018) in the sense that features are increase before activations and reduced before updating. BPP shows a workflow structure similar to the Multi-scale DenseNet architecture in (Huang et al. 2018), except in the latter scale-causality moves downwards in scale, it does not use back-projections and it focuses on a label prediction problem. The WaveNet architecture (Oord et al. 2016) also shares the property of scale causality but without back-projections, moving information upwards in scale without any step back. Finally, a

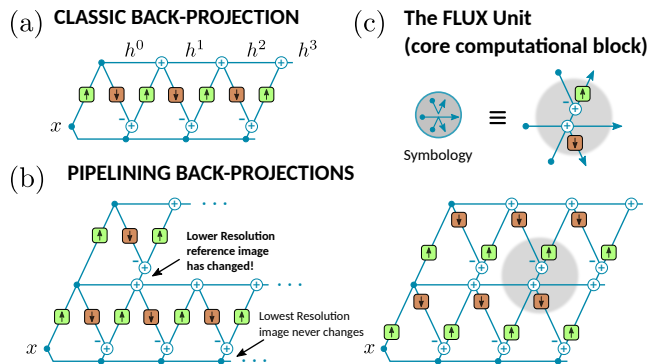


Figure 2: Pipelining Iterative Back-Projections.

similar causality and adaptation in the number of channels per scale exists in the SlowFast architecture (Feichtenhofer et al. 2019) but again without back-projections.

Contributions. Our major contribution is the introduction of a new network architecture that extends ResNets from single to multiple resolutions, with a clear representation in terms of ODE dynamic. Our main focus is to evaluate this extension and to prove that it is beneficial with respect to conventional ResNets. We also verify that the multi-scale dynamic of the network is being used to achieve improved performance and we visualize the dynamic of the network in solving different problems. BPP can be used to solve joint local problems, as well as combinations of global and local problems, getting state-of-art results in image-SR and competitive results for other problems using a single network configuration. Finally, we also show empirical evidence that BPP effectively uses both local and global information to solve problems.

Architecture Design

In Figure 2 (a) we observe the workflow of the Iterative Back-Projections (Irani and Peleg 1991) (IBP) algorithm:

$$\begin{aligned} h^0 &= P x, & h^{t+1} &= h^t + P e(h^t), \\ e(h^t) &= x - R h^t. \end{aligned} \quad (1)$$

IBP upscales an image x with a linear operator P and sends it back to low-resolution to verify the downscaling model represented by a linear operator R . Now, we propose to extend the IBP algorithm to multiple scales by using the data pipeline approach shown in Figure 2 (b). Specifically, as soon as we get the first upscale image, we take it as reference and start a new upscaling to a higher resolution. Next, we downscale the second high-resolution image to verify the downscaling model. However, the reference image has been changed by the back-projection update at the lower level. At the lowest resolution the image never changes, and upper level iterations need to keep track of the lower level updates. In Figure 2 (b) we identify the essential computational block to assemble the pipeline: the *Flux* unit. The *Flux* unit is what makes scale travel possible by connecting input and output images from different levels.

Network Architecture. Without loss of generality, we tackle the image enhancement problem with an input res-

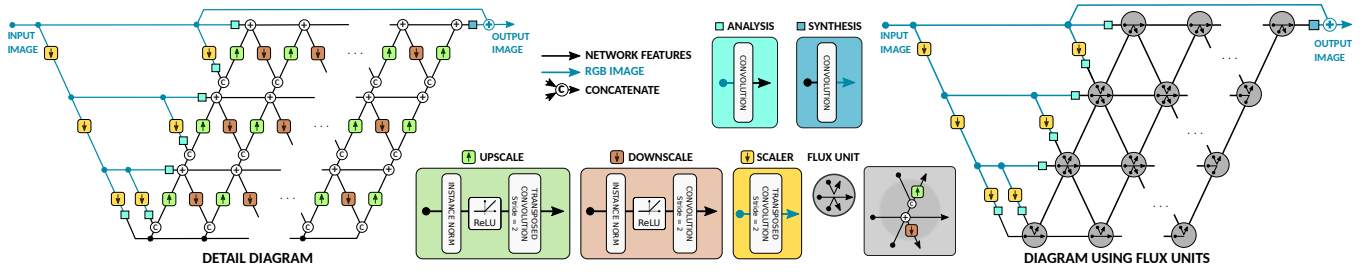


Figure 3: Back-Projection Pipeline network diagram. On the left, a detailed diagram shows all back-projection units modules. On the right, the diagram is simplified by using *Flux* units.

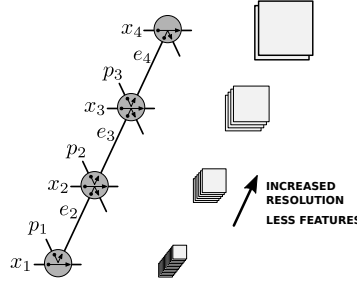
Algorithm 1 Back-Projection Pipeline (BPP)

$BPP(input, L, D)$:

Input: Image $input$.
Input: Integer $L \geq 1, D \geq 1$.
Output: Image $output$.
1: $s_L^A = input$
2: **for** $k = L - 1, \dots, 1$ **do**
3: $s_k^A = Scaler_k^A(s_{k+1}^A)$
4: **end for**
5: $x_L = Analysis_k^A(s_L^A)$
6: **for** $k = 1, \dots, L - 1$ **do**
7: $x_k = Analysis_k^A(s_k^A)$
8: $s_k^B = Scaler_k^B(s_{k+1}^B)$
9: $p_k = Analysis_k^B(s_k^B)$
10: **end for**
11: **for** $l = 1, \dots, D$ **do**
12: $x, p = FluxBlock(x, p, L)$
13: **end for**
14: $output = input + Synthesis(x_L)$

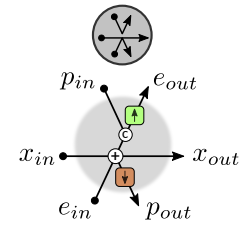
$FluxBlock(x_k, p_k, L)$:

Input: Initial $x_k, p_k, k = 1, \dots, L$.
Input: Integer $L \geq 1$.
Output: Updated $x_k, p_k, k = 1, \dots, L$.
1: $e_2, x_1, - = Flux(0, x_1, p_1)$
2: **for** $k = 2, \dots, L$ **do**
3: $e_{k+1}, x_k, p_{k-1} = Flux(e_k, x_k, p_k)$
4: **end for**
5: $-, x_L, p_{L-1} = Flux(e_L, x_L, 0)$



$Flux(e_{in}, x_{in}, p_{in})$:

Input: e_{in}, x_{in}, p_{in} .
Output: $e_{out}, x_{out}, p_{out}$.
1: $c = x_{in} + e_{in}$
2: $e_{out} = Upscale([p_{in}, c])$
3: $p_{out} = Downscale(c)$
4: $x_{out} = Update(c)$



olution equal to the output resolution. In the case of image SR, which requires to increase image resolution, we add a pre-processing stage where the input image is upscaled using a standard method (e.g. bicubic). This helps to make the system become more general for applications. For example, we can easily solve the problem of fractional up-scaling factors (Hu et al. 2019) or multiple upscaling factors (Zhang, Zuo, and Zhang 2018) by simply using different pre-processing bicubic upscalers.

The full BPP algorithm and network configuration is specified in Algorithm 1 and Figure 3. To extend the pipelining approach into a network configuration, first, we initialize the network states x_k and down-projections p_k using linear downscalers and single convolutional layers in the *Analysis* modules to increase the number of channels. Second, states are updated using the *Flux-Blocks* defined in Algorithm 1, calculating residuals e_k and updating states upwards in scale with flux units. Third, the output state in the highest resolution is converted into a residual image by a convolutional layer in the *Synthesis* module and added to the input image.

Network Dynamic. The restriction operators R_k (*Downscale* module) and interpolation operators P_k (*Upscale* module) are now non-linear and do not share parameters (time dependent). When we interpret depth as time t , the dynamic is described in Figure 4 and leads to the following set of

difference equations with their correspondent extension to continuous time:

$$\begin{aligned} h_k^{t+1} &= h_k^t + P_k(R_k(h_k^t, t), h_{k-1}^{t+1}, t) \\ h_1^{t+1} &= h_1^t, \end{aligned}$$

$\xrightarrow{\text{cont. time}}$

$$\frac{dh_k}{dt} = P_k(R_k(h_k, t), h_{k-1}, t)$$

$$h_1(x, y, t) = h_1(x, y, 0). \quad (2)$$

In the case of ResNets, the dynamical systems is given by $h^{t+1} = h^t + f(h^t, t)$ and $\frac{dh}{dt} = f(h, t)$ in continuous time. Therefore, BPP extends the model of ResNets from a single ODE to a system of coupled equations. Scale-causality follows from (2) as state h_k only depends on h_{k-1}, h_{k-2}, \dots . The multi-scale nature follows from the spatial dimension of state vectors h_k , explicitly expressed in operators $P_k : \mathbb{R}^{\frac{H}{2} \times \frac{W}{2}} \rightarrow \mathbb{R}^{H \times W}$ and $R_k : \mathbb{R}^{H \times W} \rightarrow \mathbb{R}^{\frac{H}{2} \times \frac{W}{2}}$. In continuous space we could also express the multi-scale nature of the equations by using initial conditions $h_{k-s}(x, y, t = 0) = h_k(2^s x, 2^s y, t = 0)$ with $s \in \mathbb{N}$ with no filtering needed in continuous space, since aliasing effects do not exist. We observe that initial conditions are self-similar in scale (Mallat 1998). Whether this property is maintained in time depends on the evolution of the network state. In

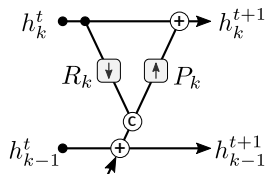


Figure 4: State diagram of the depth transitions in the BPP architecture. The residual structure leads to a non-autonomous system of differential equations.

the continuous time model, the restriction operator R_k in (2) represents a renormalization-group transformation of the network state, similar to those used in particle physics and ODEs to ensure self-similarity (Fisher 1974; Chen, Goldenfeld, and Oono 1996). In this sense, using different parameters at each scale allows the model to adjust the level of self-similarity that works better for a given problem. On the other hand, using different parameters in time can also be beneficial. It has been observed in (Liao and Poggio 2016) that normalization layers do not work well in recurrent networks, which share parameters in time. But in time-dependent systems, these layers become beneficial. Since the BPP configurations in our experiments use IN-layers, we chose to use different parameters in time. This does not have a significant effect in performance, because the flux-block structure in Algorithm 1 uses inline updates that avoid storage of old network states. During training, a checkpoint strategy can effectively reduce the memory footprint (Chen et al. 2016).

Using pipelining to extend IBP into multiple scales is simple and this is the major strength of this approach. There are several ways to extend IBP to multiple scales. We mentioned MGBP as a relevant but different approach. BPP is simpler, and that simplicity translates to a clear ODE model that is difficult to obtain otherwise. Most importantly, this ODE model is very expressive about the connection to IBP. It is direct from (2) that if the composition of P and R operations forms a contraction mapping then the ODE model will converge, which is the same argument used in convergence proofs of IBP in the linear case (Irani and Peleg 1991). At this point BPP departs from IBP. Because BPP is trained in a supervised fashion, we do not know a priori how is this dynamic going to be driven towards the target. Overall, the BPP model inherits the essence of IBP in terms of an iteration that updates residuals upwards in scale, which can now be trained to reach diverse targets in a non-linear fashion using convolutional networks. The main purpose of our investigation is: first, to generalize the IBP dynamic to multiple scales in sequence; and second, to study how powerful is this dynamic so solve more general problems.

Finally, we note that the continuous model in (2) allows BPP to work as a Neural-ODE system (Chen et al. 2018). For the sake of simplicity, in this work we do not explore this direction. However, it stands as an interesting direction for future research.

Experiments

In our experiments we found that using IN-layers to activate ReLU units, as shown in Figure 3, could help converge faster in early training and doing so independent of initialization. Figure 5 (b) shows this effect and we also see that IN-layers are not required for BPP in the long run. In early training IN layers placed before ReLUs force a 50% activation in all flux units across all scales. This strategy shows to be a good choice to initialize parameters. Alternatively, we found that the most effective way to avoid IN-layers is using Dirac-kernels to initialize weights and adding Gaussian noise. This initialization was used in the learning curve *BPP (no IN)* in Figure 5 (b) and it is the closest we have found to avoid normalization layers.

Because of memory limitations we used a patch-based training strategy, where smaller-sized patches are taken from training set images. Patch-based learning reduces the receptive field of the network during training. At inference the performance of the network reduces if the mean and variance of IN-layers are computed on an image larger than the training patches. To solve this problems we: first, divide input images into overlapping patches (of same size as training patches); second, we multiply each output by a Hamming window (Harris 1978); and third, we average the results. In all our experiments we use overlapping patches separated by 16 pixels in vertical and horizontal directions. The weighted average helps to avoid blocking artifacts.

On one hand, this approach introduces redundancy and reduces performance for medium size images. On the other hand, it also allows the algorithm to run on very large images (e.g. 8K) and can be massively parallelized by batch processing in multiple GPUs.

Configuration. In the following experiments we use a BPP configuration with 16 back-projection layers (flux-blocks), 4 resolution levels and 256, 128, 64 and 48 features per level from lowest to highest resolution, respectively. All convolutional layers use 3×3 as kernel size, and scalers are initialized with bicubic filters of size 9×9 and trained as additional parameters. A fully unrolled diagram is shown in the Appendix. The configuration was tuned according to validation performance for the most challenging problems (e.g. SR-8 \times). By fixing the configuration we can potentially have the architecture hardwired in silicon and update its model parameters to switch between different problems.

Performance. The BPP architecture is multi-scale and sequential. The so-called *Flux-Block* in Algorithm 1 represents the sequential block and consists of one Flux unit per level. This sequential structure is more convenient for memory performance as it avoids buffering of features from previous blocks. Architectures such as Dense-Nets, U-Nets and MGBP need to buffer features in skipped connections and thus need more memory. Because the configuration is fixed, the performance of the system can be roughly estimated from average statistics. The system has a total of 19 million parameters and it can process 1.7 million pixels per second on a Titan X GPU using 16-bit floating point precision. This means, for example, that it takes 3.7 seconds to process a Full-HD image in RGB format ($3 \times 1920 \times 1080$ pixels).

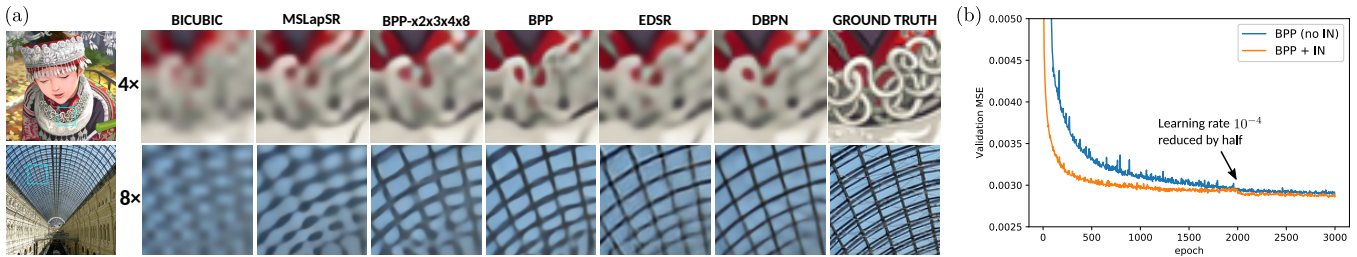


Figure 5: a) Qualitative evaluation for SR methods. b) Validation MSE for $4\times$ SR.

Table 1: Quantitative evaluation for SR. A more extensive comparison is available in the Appendix.

Algorithm	Set14		BSDS100		Urban100		Manga109	
	PSNR- Y_M	SSIM- Y_M	PSNR- Y_M	SSIM- Y_M	PSNR- Y_M	SSIM- Y_M	PSNR- Y_M	SSIM- Y_M
Bicubic	30.34	0.870	29.56	0.844	26.88	0.841	30.84	0.935
MSLapSRN	33.28	0.915	32.05	0.898	31.15	0.919	37.78	0.976
D-DBPN	33.85	0.919	32.27	0.900	32.70	0.931	39.10	0.978
EDSR	33.92	0.919	32.32	0.901	32.93	0.935	39.10	0.977
RDN	34.28	0.924	32.46	0.903	33.36	0.939	39.74	0.979
BPP-SR $\times 2\times 3\times 4\times 8$	33.27	0.913	31.21	0.879	31.67	0.921	38.31	0.975
BPP-SR $\times 2$	34.23	0.922	31.63	0.886	33.07	0.935	39.19	0.977
<hr/>								
Bicubic	27.55	0.774	27.21	0.739	24.46	0.735	26.95	0.856
MSLapSRN	29.97	0.836	28.93	0.800	27.47	0.837	32.68	0.939
EDSR	30.52	0.846	29.25	0.809	28.80	0.865	34.17	0.948
RDN	30.74	0.850	29.38	0.812	29.18	0.872	34.81	0.951
BPP-SR $\times 2\times 3\times 4\times 8$	30.23	0.838	28.81	0.794	28.43	0.852	33.75	0.943
BPP-SR $\times 3$	30.78	0.848	29.14	0.804	29.56	0.873	34.49	0.948
<hr/>								
Bicubic	26.10	0.704	25.96	0.669	23.15	0.659	24.92	0.789
MSLapSRN	28.26	0.774	27.43	0.731	25.51	0.768	29.54	0.897
D-DBPN	28.82	0.786	27.72	0.740	26.54	0.795	31.18	0.914
EDSR	28.80	0.788	27.71	0.742	26.64	0.803	31.02	0.915
RDN	29.01	0.791	27.85	0.745	27.01	0.812	31.74	0.921
BPP-SR $\times 2\times 3\times 4\times 8$	28.55	0.778	27.43	0.728	26.48	0.791	30.81	0.909
BPP-SR $\times 4$	29.07	0.791	27.89	0.745	27.55	0.819	31.63	0.918
<hr/>								
Bicubic	23.19	0.568	23.67	0.547	20.74	0.516	21.47	0.647
MSLapSRN	24.57	0.629	24.65	0.592	22.06	0.598	23.90	0.759
D-DBPN	25.13	0.648	24.88	0.601	22.83	0.622	25.30	0.799
EDSR	24.94	0.640	24.80	0.596	22.47	0.620	24.58	0.778
RDN	25.38	0.654	25.01	0.606	23.04	0.644	25.48	0.806
BPP-SR $\times 2\times 3\times 4\times 8$	25.10	0.642	24.89	0.598	22.72	0.626	24.78	0.785
BPP-SR $\times 8$	25.53	0.655	25.11	0.607	23.17	0.649	25.28	0.800

P1: Image Super-Resolution. We use DIV2K (Agustsson and Timofte 2017) and FLICKR-2K datasets for training and the following datasets for test: Set-14 (Zeyde, Elad, and Protter 2010), BSDS-100 (Martin et al. 2001), Urban-100 (Huang, Singh, and Ahuja 2015) and Manga-109 (Matsui et al. 2017). Impaired images were obtained by downscaling and then upscaling ground truth images, using Bicubic scaler, and scaling factors: $2\times$, $3\times$, $4\times$ and $8\times$. Here, we consider two cases: we trained models BPP-SR $\times f$ for each upscaling factor $f = 2, 3, 4$ and 8 ; and we also trained a single model BPP-SR $\times 2\times 3\times 4\times 8$ to restore impaired images with unknown upscaling factors. We use 16 patches per mini-batch with patch size $48f \times 48f$ for known upscaling factor f , and 192×192 for unknown upscaling factor, all at high resolution.

Table 1 and Figure 5 (a) show quantitative and qualitative results compared to other methods. We focus our comparison to the following methods: Bicubic (the baseline); EDSR (Lim et al. 2017), with major processing in 1 resolution level using a 32-layer ResNet; Dense-DBPN (Haris, Shakhnarovich, and Ukita 2018), with major processing in 2 resolution levels using 12 densely connected up/down back-

projections; and RDN (Zhang et al. 2018c), with major processing in 1 resolution level using 20 densely connected residual-dense-blocks. We show EDSR and DBPN because they are both closely related to BPP in their residual and back-projection structures, respectively, and we show RDN as a top reference of current state-of-the-arts. Further comparisons with other methods can be found in the Appendix.

Overall, for the problem of super-resolution we find that BPP can get excellent results, reaching state-of-the-arts results in both quantitative and qualitative evaluations, but it decreases its performance when we test a more general problem. First, BPP- $\times f$ models get the best scores in most quantitative and qualitative evaluations, with RDN slightly outperforming BPP at $2\times$ and $3\times$ upscaling factors. This setting, including datasets for training and test, is the most common evaluation procedure for supervised SR technics. In terms of application this would be useful if we need to enhance an image upscaled with Bicubic upscaler with a specific upscaling factor. It often happens that we have an image upscaled with an unknown factor and in this case we do not know which model parameters to load. In this case the BPP-SR $\times 2\times 3\times 4\times 8$ model offers a general upscaling

Table 2: Quantitative results of raindrop removal.

Method	PSNR- Y_P	SSIM- Y_P
Eigen13	28.59	0.6726
Pix2Pix	30.14	0.8299
DeRaindrop (No GAN)	29.25	0.7853
DeRaindrop	31.57	0.9023
BPP	30.85	0.9180

solution. This performance of these BPP models decrease and not reach state-of-the-arts results. Although reasonably close to state-of-the-arts, often outperforming EDSR, we would have expected this model to perform better than BPP- $\times f$ if the architecture was able to generalize effectively to this more general setting. In fact, it has been observed in VDSR (Kim, Lee, and Lee 2016a) and MDSR (Lim et al. 2017) that training with unknown upscaling factors can improve the performance of the network. Therefore, these empirical results show that BPP can be very effective for fixed upscaling factors but does not generalize as well as other architectures for general upscaling factors.

P2: Raindrop Removal. We use the DeRaindrop(Qian et al. 2018a,b) dataset for training and test. This dataset provides paired images, one degraded by raindrops and the other one free from raindrops. These were obtained by use two pieces of exactly the same glass: one sprayed with water, and the other is left clean. In each training batch, we take 1 patch of size 528×528 . We train a BPP model using L_1 loss and patch size 456×456 . More details of training settings are provided in the Appendix.

This problem is very different in nature to super-resolution. On one hand, a significant portion of pixels contain (uncorrupted) high-resolution information that must move to the output with little or no change. At the same time it needs to identify the irregular distribution of raindrops, with different sizes, and fill-in those areas by predicting the content within. In some images the content within raindrops is of little use, making the problem similar to inpainting. Thus, the problem requires processing of both local and global information in order to fill-in raindrops.

Even though we only trained our system with an L_1 loss, our system performs similar to the state-of-the-arts DeRaindrop (Qian et al. 2018a) as seen in Table 2 and Figure 6. The DeRaindrop network in (Qian et al. 2018a) uses an attentive GAN approach that can estimate raindrop masks to focus on these areas for restoration. The PSNR score of BPP is better than DeRaindrop without adversarial training, and the SSIM score is better than all other systems in Table 2. The qualitative evaluation shows that BPP achieves a reasonable quality, considering the fact that it has not been trained using GANs. Here, the BPP architecture appears to be effective. In the next section we inspect properties of the network that reveal the undergoing mechanism used by BPP to obtain its solutions.

Other Problems. The performance in other problems, including mobile-to-DSLR photo translation, dehaze and joint HDR+SR are included in the Appendix.

Inspection of ODE updates. We conduct experiments to measure the magnitude of the updates in equation (2) to bet-

Figure 6: Qualitative evaluation for raindrop removal.

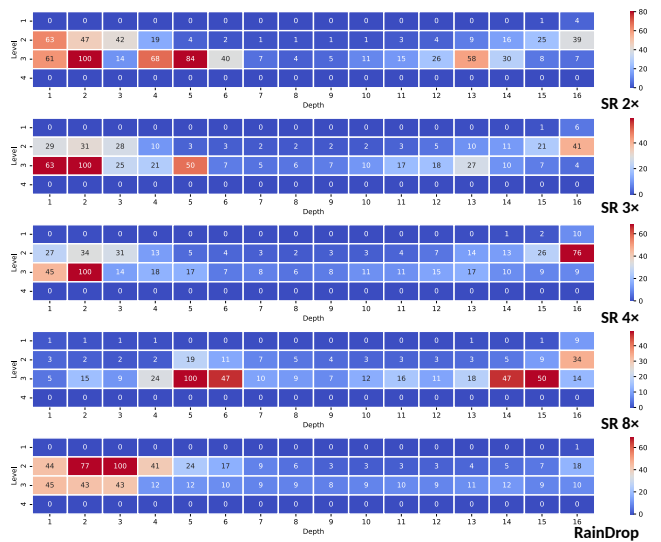
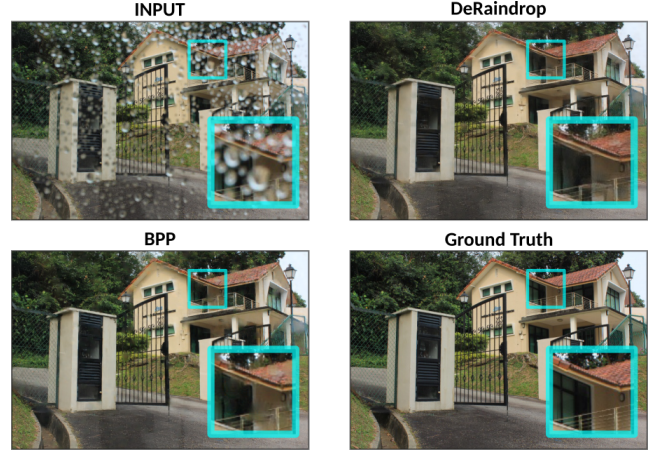


Figure 7: Average L_2 -magnitudes of residual updates normalized by the maximum update with fixed value 100.

ter understand the dynamic of the network when solving different problems. The arrange of Flux units in BPP networks forms an array of size $L \times D$ (number of levels times depth) and we compare the magnitude of residual updates in each one of these units. In Figure 7 we display the result of measuring

$$\left\| \frac{dh_k}{dt} \right\|_2 = \|P_k(R_k(h_k^t, t), h_{k-1}^{t+1}, t)\|_2, \quad (3)$$

for every flux unit, averaged over all images in the validation sets, and normalized to the maximum value (fixed to 100). At the lowest resolution ($k = 4$) the reference image never changes and thus the updates is always zero.

Interestingly, we observe that the dynamic is far from the original contraction mapping design of IBP, that would result in an exponential decay of updates along depth. Here, we should remember that the dynamic is driven exclusively by the result of training the network in supervised manner.

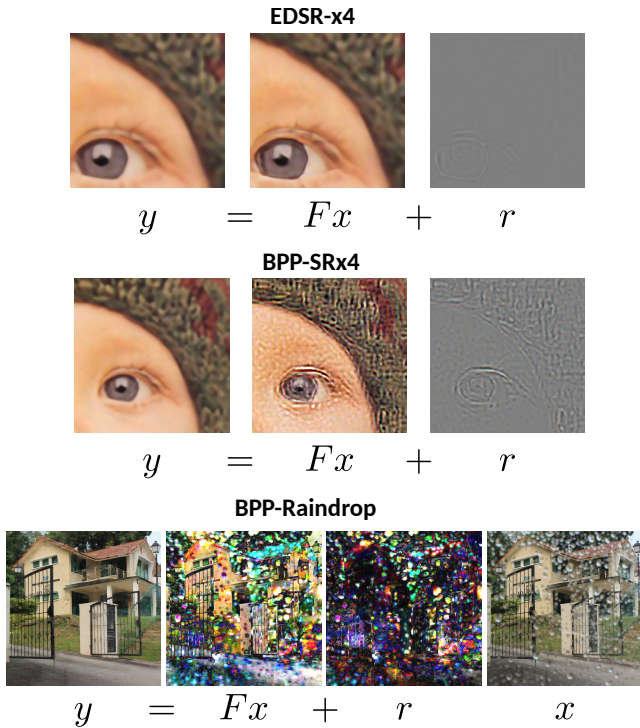


Figure 8: Local and global contributions (Fx and r) for 3 systems using deep filter visualization (Navarrete Michelini, Liu, and Zhu 2019). EDSR relies on local contributions while BPP balances both local and global contributions.

Instead of an exponential decay, the network consistently shows a bimodal statistic with one peak very close to the input and another very close to the output. Also, the highest resolution receives very small updates meaning that these feature move more or less unchanged with an increased update towards the end. The major processing goes on at the middle levels. In SR updates are stronger at the lower resolution ($k = 3$) and for RainDrop removal updates are stronger at the higher resolution ($k = 2$). The bimodal statistic is reminiscent of interpretability results for VGG networks in classification, that show higher contribution to label outputs very early and very late in a sequential configuration (Navarrete Michelini et al. 2019). Nevertheless, in BPP the updates focus on one or two resolution levels as opposed to VGG networks that are designed to process high resolutions early in the network and very low resolutions towards the end. Despite this important difference, these results suggest that sequential networks find solutions in two steps: analysis at the first layers, and fusion towards the very end.

Interpretability. We apply the *LinearScope* method from (Navarrete Michelini et al. 2019) to analyze the learning process in global and local problems. The general methodology is as follows. The BPP architecture contains several non-linear modules consisting on ReLUs and IN-layers. The decision of which pixels pass or stop in ReLUs, and what mean and variance to use in IN-layers, is non-linear. But the action of these layers are linear: masking and normalizing. For

a given input image x , the action of all non-linear modules (ReLU and IN-layers) can be fixed as: $1/0$ -masks for ReLU and fixed mean and variance in IN-layers. This gives a linear system of the form $y = Fx + r$ that generates the same output as the non-linear system for the input x , and represents the overall action of the network on the input image.

The matrix F represents the interpolation filters used by the network to solve the problem, and thus shows the *local processing*. The residual r is a fixed *global* image created by non-linear modules. Figure 8 shows the local contributions, Fx , and global contributions, r , for three systems. We observe that EDSR almost purely relies on local processing to obtain an output. BPP, on the other hand, relies mostly on local processing but the contribution of r is much larger than the one in EDSR. This shows a significantly different approach followed by BPP, compared to EDSR, to solve the super-resolution problem.

The BPP system for raindrop removal reveals a much larger contribution of r , that resembles a mask of raindrops. This means that BPP uses a local approach on areas without raindrops (using Fx) and a global approach on raindrops determined by the residual r . The mechanism used by the network to obtain the residual r is non-linear. Overall, we observe that for this problem the BPP network divides the problem in two parts: a local adaptive filter in clean areas, to nearly copy-paste the input into the output; and a non-linear global approach to fill-in raindrop areas.

Conclusions

We propose Back-Projection Pipeline as a simple yet non-trivial extension of residual networks (ResNets) to run in multiple resolutions. The update dynamic through the layers of the network includes interactions between different resolutions in a way that is causal in scale, and it is represented by a system of ODEs. We use it as a generic multi-resolution approach to enhance images. The focus of our investigation is to evaluate this multi-scale residual approach. Overall, our empirical results show that BPP can achieve excellent results in traditional supervised learning. Our BPP configuration gets state-of-the-art results in SR for fixed upscaling factors and competitive results for raindrop removal as well as other problems (see Appendix). We also observe a lack of generalization for the problem of SR with unknown upscaling factors. Inspection of the residual updates in the network shows that all resolution levels are being used, with higher intensity in lower resolutions, showing that supervised training gives preference to the multi-scale setting over traditional residual networks. Based on our results, we cannot conclude that scale causality is beneficial. Nevertheless, we can at least conclude that this strong simplification in the flow of network information, inherited from IBP, does not prevent the architecture to achieve competitive results. Further investigation is necessary in this regard (especially regarding generalization) and it could open interesting research directions in network architecture search and design.

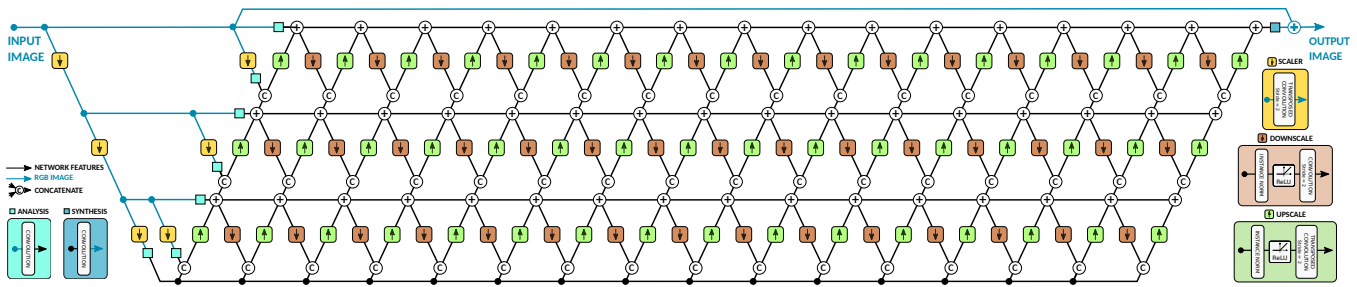


Figure 9: Detail diagram of the 4-level, 16-layers BPP configuration used in our experiments.

References

- Agustsson, E.; and Timofte, R. 2017. NTIRE 2017 Challenge on Single Image Super-Resolution: Dataset and Study. In *The IEEE Conference on Computer Vision and Pattern Recognition (CVPR) Workshops*. 5, 11
- Ancuti, C.; Ancuti, C. O.; and Timofte, R. 2019. NTIRE-2019 Dehaze Evaluation code. <https://competitions.codalab.org/my/datasets/download/a85cc0d2-cf8b-4ec8-bf83-243c7bda515>. [Online; accessed 20-May-2019]. 11
- Ancuti, C.; Ancuti, C. O.; Timofte, R.; and De Vleeschouwer, C. 2018a. I-HAZE: a dehazing benchmark with real hazy and haze-free indoor images. In *International Conference on Advanced Concepts for Intelligent Vision Systems*, 620–631. Springer. 11
- Ancuti, C.; Ancuti, C. O.; Timofte, R.; Van Gool, L.; Zhang, L.; and Yang, M. 2018b. NTIRE 2018 Challenge on Image Dehazing: Methods and Results 891–901. 1
- Ancuti, C. O.; Ancuti, C.; Sbert, M.; and Timofte, R. 2019. Dense Haze: A benchmark for image dehazing with dense-haze and haze-free images. *CoRR* abs/1904.02904. URL <http://arxiv.org/abs/1904.02904>. 11
- Ancuti, C. O.; Ancuti, C.; Timofte, R.; and De Vleeschouwer, C. 2018c. O-HAZE: a dehazing benchmark with real hazy and haze-free outdoor images. In *Proceedings of the IEEE Conference on Computer Vision and Pattern Recognition Workshops*, 754–762. 11
- Chen, L. Y.; Goldenfeld, N. D.; and Oono, Y. 1996. Renormalization group and singular perturbations: Multiple scales, boundary layers, and reductive perturbation theory. *Physical Review E* 54(1): 376–394. 4
- Chen, T.; Rubanova, Y.; Bettencourt, J.; and Duvenaud, D. K. 2018. Neural Ordinary Differential Equations. *neural information processing systems* 6571–6583. 4
- Chen, T.; Xu, B.; Zhang, C.; and Guestrin, C. 2016. Training Deep Nets with Sublinear Memory Cost. *arXiv: Learning*. 4
- Dong, C.; Loy, C. C.; He, K.; and Tang, X. 2014. Learning a Deep Convolutional Network for Image Super-Resolution. In *in Proceedings of European Conference on Computer Vision (ECCV)*. 1, 12
- Dong, C.; Loy, C. C.; and Tang, X. 2016. Accelerating the Super-Resolution Convolutional Neural Network. In *in Proceedings of European Conference on Computer Vision (ECCV)*. 12
- Ehret, T.; Davy, A.; Arias, P.; and Facciolo, G. 2019. Joint demosaicing and denoising by overfitting of bursts of raw images. 2
- Feichtenhofer, C.; Fan, H.; Malik, J.; and He, K. 2019. SlowFast Networks for Video Recognition. In *The IEEE International Conference on Computer Vision (ICCV)*. 2
- Fisher, M. E. 1974. The renormalization group in the theory of critical behavior. *Reviews of Modern Physics* 46(4): 597–616. 4
- Gharbi, M.; Chaurasia, G.; Paris, S.; and Durand, F. 2016. Deep Joint Demosaicking and Denoising. *ACM Trans. Graph.* 35(6): 191:1–191:12. ISSN 0730-0301. doi:10.1145/2980179.2982399. URL <http://doi.acm.org/10.1145/2980179.2982399>. 2
- Haris, M.; Shakhnarovich, G.; and Ukita, N. 2018. Deep Back-Projection Networks for Super-Resolution. In *IEEE Conference on Computer Vision and Pattern Recognition (CVPR)*. 5, 12
- Harris, F. J. 1978. On the use of windows for harmonic analysis with the discrete Fourier transform. *Proceedings of the IEEE* 66(1): 51–83. 4
- He, K.; Zhang, X.; Ren, S.; and Sun, J. 2016. Deep Residual Learning for Image Recognition. *computer vision and pattern recognition* 770–778. 1
- He, M.; Chen, D.; Liao, J.; Sander, P. V.; and Yuan, L. 2018. Deep exemplar-based colorization. *ACM Transactions on Graphics (TOG)* 37(4): 47. 1
- Hu, J.; Shen, L.; and Sun, G. 2018. Squeeze-and-Excitation Networks. *computer vision and pattern recognition* 7132–7141. 1
- Hu, X.; Mu, H.; Zhang, X.; Wang, Z.; Tan, T.; and Sun, J. 2019. Meta-SR: A Magnification-Arbitrary Network for Super-Resolution. *arXiv: Computer Vision and Pattern Recognition*. 3
- Huang, G.; Chen, D.; Li, T.; Wu, F.; Der Maaten, L. V.; and Weinberger, K. Q. 2018. Multi-Scale Dense Networks for Resource Efficient Image Classification. *International Conference on Learning Representations*. 2
- Huang, G.; Liu, Z.; van der Maaten, L.; and Weinberger, K. Q. 2017. Densely connected convolutional networks. In *Proceedings of the IEEE Conference on Computer Vision and Pattern Recognition*. 1, 10
- Huang, J.; Singh, A.; and Ahuja, N. 2015. Single image super-resolution from transformed self-exemplars 5197–5206. 5, 11
- Ignatov, A.; Kobyshev, N.; Timofte, R.; Vanhoey, K.; and Van Gool, L. 2017. DSLR-quality photos on mobile devices with deep convolutional networks. In *Proceedings of the IEEE International Conference on Computer Vision*, 3277–3285. 11
- Irani, M.; and Peleg, S. 1991. Improving Resolution by Image Registration. *CVGIP: Graph. Models Image Process.* 53(3): 231–239. ISSN 1049-9652. doi:10.1016/1049-9652(91)90045-L. URL [http://dx.doi.org/10.1016/1049-9652\(91\)90045-L](http://dx.doi.org/10.1016/1049-9652(91)90045-L). 2, 4
- Kim, J.; Lee, J. K.; and Lee, K. M. 2016a. Accurate Image Super-Resolution Using Very Deep Convolutional Networks. In *The IEEE Conference on Computer Vision and Pattern Recognition*. 6, 12

- Kim, J.; Lee, J. K.; and Lee, K. M. 2016b. Deeply-Recursive Convolutional Network for Image Super-Resolution. In *The IEEE Conference on Computer Vision and Pattern Recognition*. 12
- Kim, S. Y.; Oh, J.; and Kim, M. 2019. Deep SR-ITM: Joint Learning of Super-Resolution and Inverse Tone-Mapping for 4K UHD HDR Applications. In *The IEEE International Conference on Computer Vision (ICCV)*. 2
- Kingma, D. P.; and Ba, J. 2015. Adam: A method for stochastic optimization. *international conference on learning representations*. 11, 17
- Kinoshita, Y.; and Kiya, H. 2019. Convolutional Neural Networks Considering Local and Global features for Image Enhancement. In *The IEEE International Conference on Image Processing (ICIP)*. 2
- Kokkinos, F.; and Lefkimmiatis, S. 2018. Deep image demosaicking using a cascade of convolutional residual denoising networks. In *Proceedings of the European Conference on Computer Vision (ECCV)*, 303–319. 1
- Kundu, D.; Ghadiyaram, D.; Bovik, A. C.; and Evans, B. L. 2017a. Evaluation code for HIGRADE metric. <http://live.ece.utexas.edu/research/Quality/higradeRelease.zip>. [Online; accessed 20-May-2019]. 10, 11
- Kundu, D.; Ghadiyaram, D.; Bovik, A. C.; and Evans, B. L. 2017b. No-Reference Quality Assessment of Tone-Mapped HDR Pictures. *IEEE Transactions on Image Processing* 26(6): 2957–2971. 10, 11
- Lai, W.; Huang, J.; Ahuja, N.; and Yang, M. 2018. Fast and Accurate Image Super-Resolution with Deep Laplacian Pyramid Networks. *IEEE Transactions on Pattern Analysis and Machine Intelligence* 31(3): 2599–2613. 12
- Lai, W.-S.; Huang, J.-B.; Ahuja, N.; and Yang, M.-H. 2017. Deep Laplacian Pyramid Networks for Fast and Accurate Super-Resolution. In *IEEE Conference on Computer Vision and Pattern Recognition*. 12
- Lefkimmiatis, S. 2018. Universal denoising networks: a novel CNN architecture for image denoising. In *Proceedings of the IEEE Conference on Computer Vision and Pattern Recognition*, 3204–3213. 1
- Liao, Q.; and Poggio, T. 2016. Bridging the gaps between residual learning, recurrent neural networks and visual cortex. *arXiv preprint arXiv:1604.03640*. 1, 4
- Lim, B.; Son, S.; Kim, H.; Nah, S.; and Lee, K. M. 2017. Enhanced Deep Residual Networks for Single Image Super-Resolution. In *The IEEE Conference on Computer Vision and Pattern Recognition (CVPR) Workshops*. 1, 5, 6, 11, 12
- Lindeberg, T. 1994. *Scale-Space Theory in Computer Vision*. ISBN 0-7923-9418-6. doi:10.1007/978-1-4757-6465-9. 1
- Lu, G.; Ouyang, W.; Xu, D.; Zhang, X.; Gao, Z.; and Sun, M.-T. 2018. Deep Kalman filtering network for video compression artifact reduction. In *Proceedings of the European Conference on Computer Vision (ECCV)*, 568–584. 1
- Ma, C.; Yang, C.-Y.; Yang, X.; and Yang, M.-H. 2017. Learning a No-Reference Quality Metric for Single-Image Super-Resolution. *Computer Vision and Image Understanding* 1–16. 11
- Ma, C.; Yang, C.-Y.; Yang, X.; and Yang, M.-H. 2018. Evaluation code for Ma-metric. <https://github.com/chaoma99/sr-metric>. [Online; accessed 20-May-2019]. 11
- Mallat, S. 1998. *A Wavelet Tour of Signal Processing*. Academic Press. 1, 3
- Martin, D. R.; Fowlkes, C. C.; Tal, D.; and Malik, J. 2001. A database of human segmented natural images and its application to evaluating segmentation algorithms and measuring ecological statistics 2: 416–423. 5, 11
- Matsui, Y.; Ito, K.; Aramaki, Y.; Fujimoto, A.; Ogawa, T.; Yamasaki, T.; and Aizawa, K. 2017. Sketch-based manga retrieval using manga109 dataset. *Multimedia Tools and Applications* 76(20): 21811–21838. 5, 11
- Navarrete Micheline, P.; Liu, H.; Lu, Y.; and Jiang, X. 2019. A Tour of Convolutional Networks Guided by Linear Interpreters. In *The IEEE International Conference on Computer Vision (ICCV)*. IEEE. URL <https://arxiv.org/abs/1908.05168>. 7
- Navarrete Micheline, P.; Liu, H.; and Zhu, D. 2019. Multigrid Back-projection Super-Resolution and Deep Filter Visualization. In *Proceedings of the Thirty-Third AAAI Conference on Artificial Intelligence (AAAI 2019)*. AAAI. 2, 7, 12
- Nemoto, H.; Korshunov, P.; Hanhart, P.; and Ebrahimi, T. 2015. Visual attention in LDR and HDR images. Technical report. URL <https://mmspg.epfl.ch/downloads/hdr-eye/>. 11
- Oord, A. v. d.; Dieleman, S.; Zen, H.; Simonyan, K.; Vinyals, O.; Graves, A.; Kalchbrenner, N.; Senior, A.; and Kavukcuoglu, K. 2016. Wavenet: A generative model for raw audio. *arXiv preprint arXiv:1609.03499*. 2
- Paszke, A.; Gross, S.; Chintala, S.; Chanan, G.; Yang, E.; DeVito, Z.; Lin, Z.; Desmaison, A.; Antiga, L.; and Lerer, A. 2017. Automatic differentiation in PyTorch. In *NIPS-W*. 17
- Poggio, T.; Mhaskar, H.; Rosasco, L.; Miranda, B.; and Liao, Q. 2017. Why and when can deep-but not shallow-networks avoid the curse of dimensionality: a review. *International Journal of Automation and Computing* 14(5): 503–519. 1
- Qian, G.; Gu, J.; Ren, J. S.; Dong, C.; Zhao, F.; and Lin, J. 2019. Trinity of Pixel Enhancement: a Joint Solution for Demosaicking, Denoising and Super-Resolution. *arXiv e-prints arXiv:1905.02538*. 2
- Qian, R.; Tan, R. T.; Yang, W.; Su, J.; and Liu, J. 2018a. Attentive Generative Adversarial Network for Raindrop Removal From a Single Image. In *The IEEE Conference on Computer Vision and Pattern Recognition (CVPR)*. 1, 6, 17
- Qian, R.; Tan, R. T.; Yang, W.; Su, J.; and Liu, J. 2018b. De-Raindrop dataset. <https://drive.google.com/open?id=1e7R76s6vwUJxILOcAsthgDLPsNrQ49K>. [Online; accessed 20-May-2019]. 6, 17
- Qian, R.; Tan, R. T.; Yang, W.; Su, J.; and Liu, J. 2018c. Evaluation code for Raindrop removal. <https://github.com/rui1996/DeRaindrop/blob/master/metrics.py>. [Online; accessed 20-May-2019]. 11
- Reinhard, E.; and Devlin, K. 2005. Dynamic range reduction inspired by photoreceptor physiology. *IEEE Transactions on Visualization and Computer Graphics* 11(1): 13–24. 11
- Ronneberger, O.; Fischer, P.; and Brox, T. 2015. U-Net: Convolutional Networks for Biomedical Image Segmentation. *medical image computing and computer assisted intervention* 234–241. 1, 2
- Soh, J. W.; Park, J. S.; and Cho, N. I. 2019. Joint High Dynamic Range Imaging and Super-Resolution from a Single Image. *arXiv:1905.00933 [cs, eess]* URL <http://arxiv.org/abs/1905.00933>. ArXiv: 1905.00933. 2, 11
- Tao, X.; Gao, H.; Shen, X.; Wang, J.; and Jia, J. 2018. Scale-recurrent Network for Deep Image Deblurring. In *IEEE Conference on Computer Vision and Pattern Recognition (CVPR)*. 1

Timofte, R.; Gu, S.; Wu, J.; Van Gool, L.; Zhang, L.; Yang, M.-H.; and et al. 2018. NTIRE 2018 Challenge on Single Image Super-Resolution: Methods and Results. In *The IEEE Conference on Computer Vision and Pattern Recognition (CVPR) Workshops*. 1

Timofte, R.; and Smet, V. D. 2014. Gool, “A+: Adjusted anchored neighborhood regression for fast super-resolution. In *in Proc. Asian Conf. Comput. Vis. (ACCV)*. 12

Trottenberg, U.; and Schuller, A. 2001. *Multigrid*. Orlando, FL, USA: Academic Press, Inc. ISBN 0-12-701070-X. 2

Wang, S.; Zheng, J.; Hu, H.-M.; and Li, B. 2013. Naturalness preserved enhancement algorithm for non-uniform illumination images. *IEEE Transactions on Image Processing* 22(9): 3538–3548. 11

Wang, T.; Yang, X.; Xu, K.; Chen, S.; Zhang, Q.; and Lau, R. 2019. Spatial Attentive Single-Image Deraining with a High Quality Real Rain Dataset. *arXiv preprint arXiv:1904.01538*. 1

Wang, X.; Girshick, R. B.; Gupta, A.; and He, K. 2018. Non-local Neural Networks. *computer vision and pattern recognition* 7794–7803. 1

Wu, S.; Xu, J.; Tai, Y.-W.; and Tang, C.-K. 2018. Deep High Dynamic Range Imaging with Large Foreground Motions. In *The European Conference on Computer Vision (ECCV)*. 1

Yu, J.; Fan, Y.; Yang, J.; Xu, N.; Wang, Z.; Wang, X.; and Huang, T. S. 2018. Wide Activation for Efficient and Accurate Image Super-Resolution. *arXiv: Computer Vision and Pattern Recognition*. 2

Zeyde, R.; Elad, M.; and Protter, M. 2010. On single image scale-up using sparse-representations 711–730. 5, 11

Zhang, H.; Sindagi, V.; and Patel, V. M. 2018. Multi-scale Single Image Dehazing using Perceptual Pyramid Deep Network. In *The IEEE Conference on Computer Vision and Pattern Recognition (CVPR) Workshops*. 11

Zhang, K.; Zuo, W.; and Zhang, L. 2018. Learning a Single Convolutional Super-Resolution Network for Multiple Degradations. *computer vision and pattern recognition* 3262–3271. 2, 3

Zhang, Y.; Li, K.; Li, K.; Wang, L.; Zhong, B.; and Fu, Y. 2018a. Image super-resolution using very deep residual channel attention networks. In *Proceedings of the European Conference on Computer Vision (ECCV)*, 286–301. 1, 12

Zhang, Y.; Li, K.; Li, K.; Zhong, B.; and Fu, Y. 2019. Residual Non-local Attention Networks for Image Restoration. *international conference on learning representations*. 1, 2

Zhang, Y.; Tian, Y.; Kong, Y.; Zhong, B.; and Fu, Y. 2018b. Evaluation code for Residual Dense Networks. https://github.com/yulunzhang/RDN/blob/master/RDN_TestCode/Evaluate_PSNR_SSIM.m. [Online; accessed 20-May-2019]. 11

Zhang, Y.; Tian, Y.; Kong, Y.; Zhong, B.; and Fu, Y. 2018c. Residual Dense Network for Image Restoration. 5, 12

Zhang, Y.; Tian, Y.; Kong, Y.; Zhong, B.; and Fu, Y. 2018d. Residual Dense Network for Image Super-Resolution. In *CVPR*. 1

Appendix

Diagrams

In an effort to make diagrams easy to read, concise and carrying a precise meaning, we introduce the notation in Figure 10. This is, lines connected to the left-side of any given module represent different inputs to that module. Every module can have several inputs but only one output.

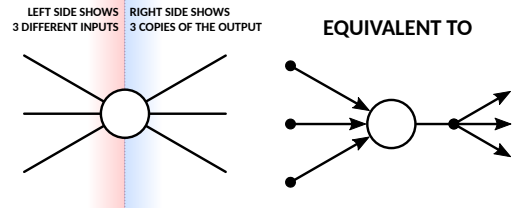


Figure 10: Diagram notation.

Lines connected to the right-side of a given module represent copies of the same output.

Figure 9 shows an expanded diagram of the single BPP configuration used in our experiments. It uses 16 back-projection layers (flux blocks), 4 resolution levels and 256, 128, 64 and 48 features per level from lowest to highest resolution, respectively. All convolutional layers use 3×3 as kernel size, and scalars are initialized with bicubic filters of size 9×9 and trained as additional parameters.

We observe that, after initialization, the lowest-resolution network state (at the bottom of the diagram) never changes. Thus, the highest-resolution state (at the top of the diagram) is always 3-layers away from this fixed state. This is similar to a long-range skip-connection in DenseNet (Huang et al. 2017), but in BPP these shortcut moves through a different resolution. Because of scale causality, the next low-resolution level moves relatively close to the fixed state and we can interpret it as a shorter-range skip-connection. Thus, the particular structure of BPP allows quick paths from the output to every layer of the network, similar to DenseNets, which is convenient for the gradient flow during back-propagation steps.

Evaluation Metrics

Quantitative evaluations in our experiments include three objective metrics: PSNR, SSIM and HIGRADE-2. From these, PSNR and SSIM are reference-based metrics that measure the difference between an impaired image and ground truth. Higher values are better in both cases. The PSNR (range 0 to ∞) is a log-scale version of mean-square-error and SSIM (range 0 to 1) uses image statistics to better correlate with human perception. Full expressions are as follows:

$$PSNR(X, Y) = 10 \cdot \log_{10} \left(\frac{255^2}{MSE} \right), \quad (4)$$

$$SSIM(X, Y) = \frac{(2\mu_X\mu_Y + c_1)(2\sigma_{XY} + c_2)}{(\mu_X^2 + \mu_Y^2 + c_1)(\sigma_X^2 + \sigma_Y^2 + c_2)}, \quad (5)$$

where $MSE = \mathbb{E}[(X - Y)^2]$ is the mean square error of the difference between X and Y ; μ_X and μ_Y are the averages of X and Y , respectively; σ_X^2 and σ_Y^2 are the variances of X and Y , respectively; σ_{XY} is the covariance of X and Y ; $c_1 = 6.5025$ and $c_2 = 58.5225$.

HIGRADE-2(Kundu et al. 2017b) is a non-reference image quality metric based on gradient scene-statistics defined in the LAB color space and it is often used to evaluate high-dynamic-range images. Here, we used the Matlab code available in (Kundu et al. 2017a).

In the case of PSNR and SSIM metrics, we follow existing benchmarks that use different versions of these metrics. We used the following three definitions in our experiments:

- **PSNR/SSIM – Y_M** : Based on the Matlab code available in (Zhang et al. 2018b), computes PSNR/SSIM on the Y channel. Matlab uses a conversion of RGB to YUV color-spaces following the BT.709 standard, including offsets that are often avoided in other implementations.
- **PSNR/SSIM – Y_P** : Based on the Python code available in (Qian et al. 2018c), computes PSNR/SSIM on the Y channel. The code uses an OpenCV function to convert from RGB to YCbCr color-space.
- **PSNR/SSIM – RGB**: Based on the Python code available in (Ancuti, Ancuti, and Timofte 2019), computes the average PSNR/SSIM for pairs of RGB images.

Training Settings

Image Super-Resolution We use DIV2K(Agustsson and Timofte 2017) and FLICKR-2K datasets for training and the following datasets for test: Set-14(Zeyde, Elad, and Protter 2010), BSDS-100(Martin et al. 2001), Urban-100(Huang, Singh, and Ahuja 2015) and Manga-109(Matsui et al. 2017). Impaired images were obtained by downscaling and then upscaling ground truth images, using Bicubic scaler, with scaling factors: $2\times$, $3\times$, $4\times$ and $8\times$. Our target is to recover the ground truth so we use a loss function that measures the L_1 distance between impaired images and ground truth. For evaluation we measure PSNR and SSIM on the Y -channel using the Matlab code from (Zhang et al. 2018b).

We follow the training settings from (Lim et al. 2017). In each training batch, we randomly take 16 impaired patches from our training set (800 DIV2K plus 2,650 FLICKR-2K images). We consider two cases: we train a model BPP-SR $\times f$ for each upscaling factor $f = 2, 3, 4$ and 8; and we also train a model BPP-SR $\times 2\times 3\times 4\times 8$ to restore impaired images with unknown upscaling factor. We use patch size $48f \times 48f$, for $f = 2, 3$ and 4, and 192×192 for $f = 8$ and unknown upscaling factor. We augment the patches by random horizontal/vertical flipping and rotating 90° . We use Adam optimizer(Kingma and Ba 2015) with learning rate initialized to 10^{-4} and decreased by half every 200,000 back-propagation steps.

The training data used for the BPP-SR $\times 2\times 3\times 4\times 8$ model includes all images used for training the upscaling factors $f = 2, 3, 4$ and 8. We could have chosen to train our model using a random and fractional upscaling factor $2.0 \leq f \leq 8.0$, but this would have made it difficult to reproduce the training settings.

Mobile-to-DSLR Photo Translation We use the DPED(Ignatov et al. 2017) dataset for training and test. This dataset provides 100×100 aligned patches taken from iPhone-mobile photos (impaired) and DSLR-Canon photos (ground truth). There are 160,471 patches available for training and 4,353 patches for test. We take 400 patches from the test set for validation during training. We use full size iPhone images from DPED for qualitative results. For

loss function we use the negative SSIM between impaired and ground truth patches. We find SSIM to be more effective than L_1 and MSE losses in this problem. For evaluation we measure the average PSNR and SSIM metrics for RGB pairs, using the code from (Ancuti, Ancuti, and Timofte 2019), and the non-reference metric HIGRADE-2(Kundu et al. 2017b) using the Matlab code available from (Kundu et al. 2017a).

In each training batch, we take 16 patches of size 100×100 . We use Adam optimizer(Kingma and Ba 2015) with learning rate initialized to 10^{-4} and decreased by half every 200,000 back-propagation steps. We do not observe improvements after 200 epochs.

Image Dehaze We use the following real haze datasets: I-Haze(Ancuti et al. 2018a), O-Haze(Ancuti et al. 2018c) and Dense-Haze(Ancuti et al. 2019). We follow the training setting from (Zhang, Sindagi, and Patel 2018). In each training batch, we take 1 patch of size 528×528 . The training set is augmented by rescaling the images, using bicubic scaler, to $1.25\times$, $1\times$, $0.625\times$ and $0.3125\times$ the original size. We use Adam optimizer(Kingma and Ba 2015) with learning rate initialized to 10^{-4} and decreased by half every 200,000 back-propagation steps. We train the system for 10,000 epochs.

Joint HDR and Super-Resolution We use the HDR-Eye(Nemoto et al. 2015) dataset for training and Wang LDR(Wang et al. 2013) dataset for test. HDR-Eye(Nemoto et al. 2015) provides HDR images constructed from multi-exposure photographs. Following the training configuration in (Soh, Park, and Cho 2019), we select 40 from a total of 46 standard-exposed and HDR-constructed pairs of images (we excluded images C01.png, C04.png, C13.png, C28.png, C38.png and C42.png, because of visible misalignment problems in the HDR image constructions). Then, we take each standard-exposed image and we: first, downscale it by factor 2; and then upscale it by factor 2 (both with bicubic scaler), and use this output as impaired image. We follow the configuration in (Soh, Park, and Cho 2019) although their tone-mapping algorithms are not specified and tone-mapped images are not provided. We use several tone-mapping algorithms until being able to produce competitive quantitative and qualitative outputs. For our final results we used the OpenCV implementation of Reinhard-Devlin tone-mapping (Reinhard and Devlin 2005) with parameters $\gamma = 2.2$, $\text{intensity} = 0$, $\text{light_adapt} = 0$. and $\text{color_adapt} = 0$.

We train our system using patches of size 456×456 . Following the analysis in (Soh, Park, and Cho 2019), we use the non-reference image quality metrics: Ma(Ma et al. 2017, 2018), to evaluate SR improvements; and HIGRADE-2(Kundu et al. 2017b,a) to evaluate HDR improvements. We augment the patches by random horizontal/vertical flipping and rotating 90° . We use Adam optimizer(Kingma and Ba 2015) with learning rate initialized to 10^{-4} and decreased by half every 200,000 back-propagation steps. We train the system for 10,000 epochs.

Table 3: Extended quantitative evaluation for super-resolution.

Algorithm	Set14		BSDS100		Urban100		Manga109	
	PSNR- Y_M	SSIM- Y_M	PSNR- Y_M	SSIM- Y_M	PSNR- Y_M	SSIM- Y_M	PSNR- Y_M	SSIM- Y_M
Bicubic	30.34	0.870	29.56	0.844	26.88	0.841	30.84	0.935
A+ (Timofte and Smet 2014)	32.40	0.906	31.22	0.887	29.23	0.894	35.33	0.967
FSRCNN (Dong, Loy, and Tang 2016)	32.73	0.909	31.51	0.891	29.87	0.901	36.62	0.971
SRCNN (Dong et al. 2014)	32.29	0.903	31.36	0.888	29.52	0.895	35.72	0.968
MSLapSRN (Lai et al. 2018)	33.28	0.915	32.05	0.898	31.15	0.919	37.78	0.976
VDSR (Kim, Lee, and Lee 2016a)	32.97	0.913	31.90	0.896	30.77	0.914	37.16	0.974
LapSRN (Lai et al. 2017)	33.08	0.913	31.80	0.895	30.41	0.910	37.27	0.974
DRCN (Kim, Lee, and Lee 2016b)	32.98	0.913	31.85	0.894	30.76	0.913	37.57	0.973
MGBP (Navarrete Michelini, Liu, and Zhu 2019)	33.27	0.915	31.99	0.897	31.37	0.920	37.92	0.976
D-DBPN (Haris, Shakhnarovich, and Ukita 2018)	33.85	0.919	32.27	0.900	32.70	0.931	39.10	0.978
EDSR (Lim et al. 2017)	33.92	0.919	32.32	0.901	32.93	0.935	39.10	0.977
RDN (Zhang et al. 2018c)	34.28	0.924	32.46	0.903	33.36	0.939	39.74	0.979
RCAN (Zhang et al. 2018a)	34.12	0.921	32.41	0.903	33.34	0.938	39.44	0.979
BPP-SRx2x3x4x8	33.27	0.913	31.21	0.879	31.67	0.921	38.31	0.975
BPP-SRx2	34.23	0.922	31.63	0.886	33.07	0.935	39.19	0.977
Bicubic	27.55	0.774	27.21	0.739	24.46	0.735	26.95	0.856
SRCNN (Dong et al. 2014)	29.30	0.822	28.41	0.786	26.24	0.799	30.48	0.912
MSLapSRN (Lai et al. 2018)	29.97	0.836	28.93	0.800	27.47	0.837	32.68	0.939
LapSRN (Lai et al. 2017)	29.87	0.832	28.82	0.798	27.07	0.828	32.21	0.935
EDSR (Lim et al. 2017)	30.52	0.846	29.25	0.809	28.80	0.865	34.17	0.948
RDN (Zhang et al. 2018c)	30.74	0.850	29.38	0.812	29.18	0.872	34.81	0.951
BPP-SRx2x3x4x8	30.23	0.838	28.81	0.794	28.43	0.852	33.75	0.943
BPP-SRx3	30.78	0.848	29.14	0.804	29.56	0.873	34.49	0.948
Bicubic	26.10	0.704	25.96	0.669	23.15	0.659	24.92	0.789
A+ (Timofte and Smet 2014)	27.43	0.752	26.82	0.710	24.34	0.720	27.02	0.850
FSRCNN (Dong, Loy, and Tang 2016)	27.70	0.756	26.97	0.714	24.61	0.727	27.89	0.859
SRCNN (Dong et al. 2014)	27.61	0.754	26.91	0.712	24.53	0.724	27.66	0.858
MSLapSRN (Lai et al. 2018)	28.26	0.774	27.43	0.731	25.51	0.768	29.54	0.897
VDSR (Kim, Lee, and Lee 2016a)	28.03	0.770	27.29	0.726	25.18	0.753	28.82	0.886
LapSRN (Lai et al. 2017)	28.19	0.772	27.32	0.728	25.21	0.756	29.09	0.890
DRCN (Kim, Lee, and Lee 2016b)	28.04	0.770	27.24	0.724	25.14	0.752	28.97	0.886
MGBP (Navarrete Michelini, Liu, and Zhu 2019)	28.43	0.778	27.42	0.732	25.70	0.774	30.07	0.904
D-DBPN (Haris, Shakhnarovich, and Ukita 2018)	28.82	0.786	27.72	0.740	26.54	0.795	31.18	0.914
EDSR (Lim et al. 2017)	28.80	0.788	27.71	0.742	26.64	0.803	31.02	0.915
RDN (Zhang et al. 2018c)	29.01	0.791	27.85	0.745	27.01	0.812	31.74	0.921
RCAN (Zhang et al. 2018a)	28.87	0.789	27.77	0.744	26.82	0.809	31.22	0.917
BPP-SRx2x3x4x8	28.55	0.778	27.43	0.728	26.48	0.791	30.81	0.909
BPP-SRx4	29.07	0.791	27.89	0.745	27.55	0.819	31.63	0.918
Bicubic	23.19	0.568	23.67	0.547	20.74	0.516	21.47	0.647
A+ (Timofte and Smet 2014)	23.98	0.597	24.20	0.568	21.37	0.545	22.39	0.680
FSRCNN (Dong, Loy, and Tang 2016)	23.93	0.592	24.21	0.567	21.32	0.537	22.39	0.672
SRCNN (Dong et al. 2014)	23.85	0.593	24.13	0.565	21.29	0.543	22.37	0.682
MSLapSRN (Lai et al. 2018)	24.57	0.629	24.65	0.592	22.06	0.598	23.90	0.759
VDSR (Kim, Lee, and Lee 2016a)	24.21	0.609	24.37	0.576	21.54	0.560	22.83	0.707
LapSRN (Lai et al. 2017)	24.44	0.623	24.54	0.586	21.81	0.582	23.39	0.735
MGBP (Navarrete Michelini, Liu, and Zhu 2019)	24.82	0.635	24.67	0.592	22.21	0.603	24.12	0.765
D-DBPN (Haris, Shakhnarovich, and Ukita 2018)	25.13	0.648	24.88	0.601	22.83	0.622	25.30	0.799
EDSR (Lim et al. 2017)	24.94	0.640	24.80	0.596	22.47	0.620	24.58	0.778
RDN (Zhang et al. 2018c)	25.38	0.654	25.01	0.606	23.04	0.644	25.48	0.806
RCAN (Zhang et al. 2018a)	25.23	0.651	24.98	0.606	23.00	0.645	25.24	0.803
BPP-SRx2x3x4x8	25.10	0.642	24.89	0.598	22.72	0.626	24.78	0.785
BPP-SRx8	25.53	0.655	25.11	0.607	23.17	0.649	25.28	0.800

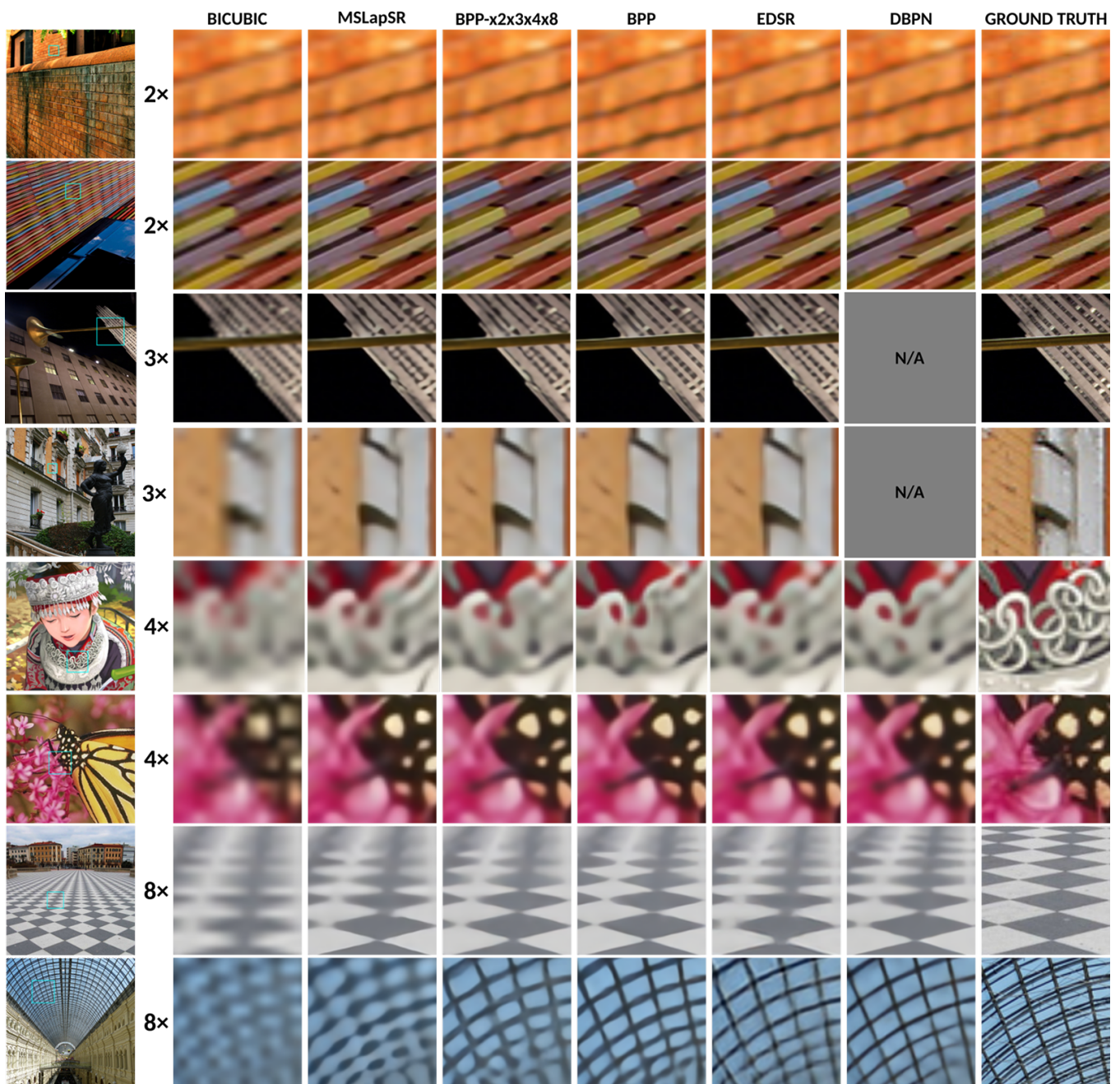


Figure 11: Extended qualitative evaluation for super-resolution.

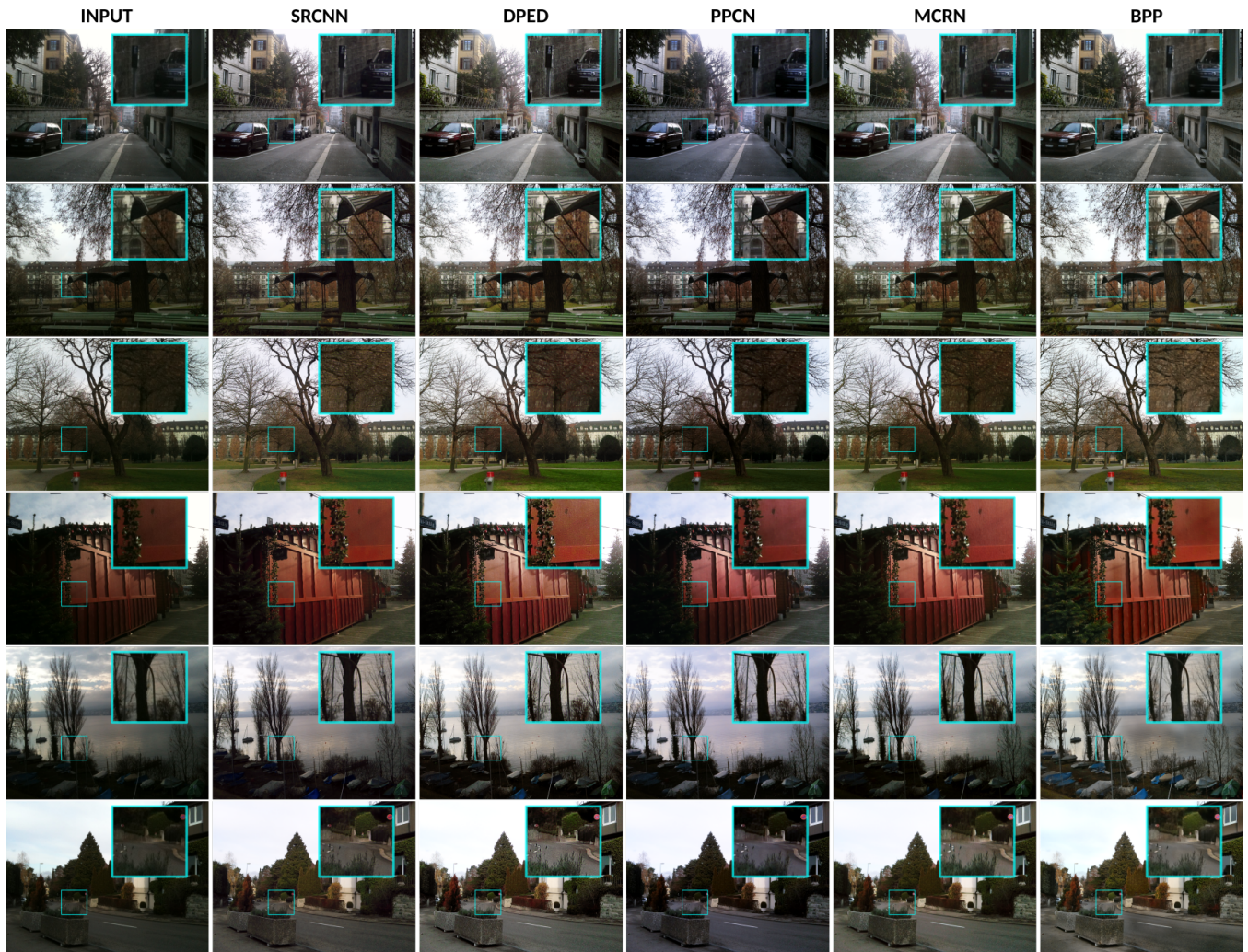


Figure 12: Extended qualitative evaluation for Mobile-to-DSLR photo translation.



Figure 13: Extended qualitative evaluation for image dehaze for Indoor/Outdoor datasets.

DENSE



Figure 14: Extended qualitative evaluation for image dehazing for Dense dataset.

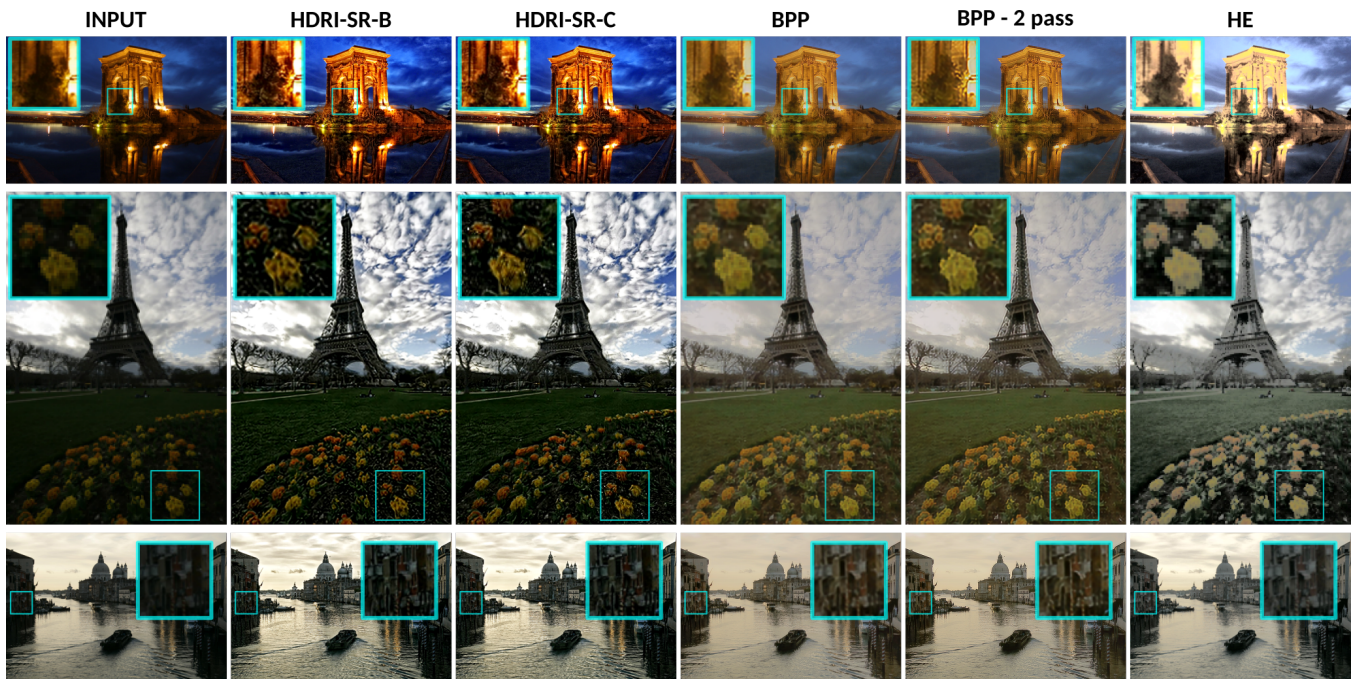


Figure 15: Extended qualitative evaluation for joint HDR+SR enhancement.

Raindrop Removal We use the DeRaindrop(Qian et al. 2018a,b) dataset for training and test. This dataset provides paired images, one degraded by raindrops and the other one free from raindrops. In each training batch, we take 1 patch of size 528×528 . We train a BPP model using L_1 loss and patch size 456×456 . We use Adam optimizer(Kingma and Ba 2015) with learning rate initialized to 10^{-4} and decreased by half every 200,000 back-propagation steps. We train the system for 10,000 epochs.

Computing Infrastructure

All training processes run on Linux operating system, using implementations in Python language with software packages: Numpy, Pytorch(Paszke et al. 2017), Scilab, Pillow and OpenCV. We used NVIDIA Tesla M40 (24GB) GPU for training and NVIDIA Titan-X Maxwell (12GB) for tests.

Reproducibility

All output images of the BPP systems obtained in our experiments can be downloaded from the following [link \(2.77 GB\)](#) This can be used to reproduce all quantitative evaluations in our experiments. We have provided external links to all evaluation scripts used in our evaluations.

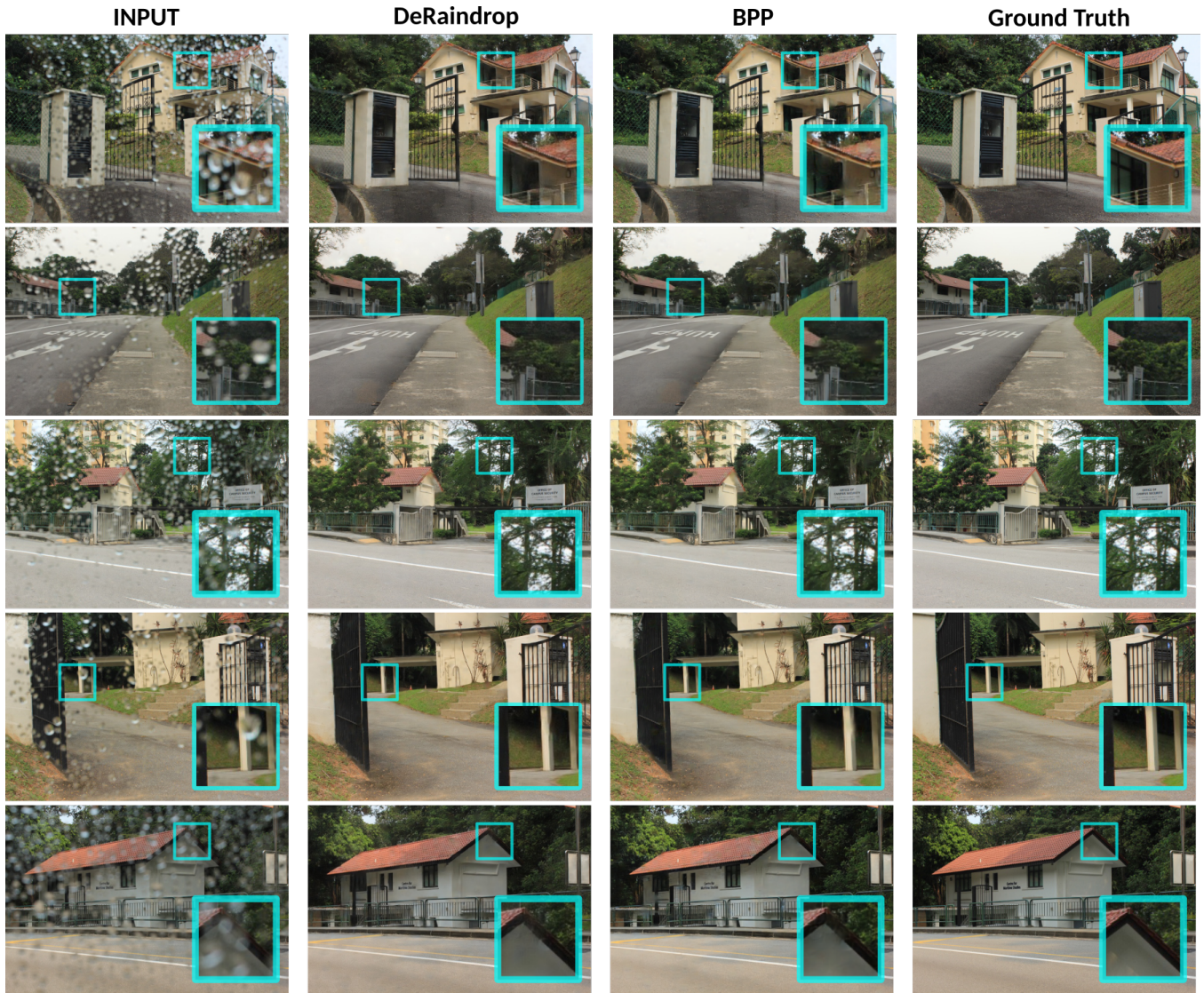


Figure 16: Extended qualitative evaluation for raindrop removal.